JACS
JOURNAL OF THE AMERICAN CHEMICAL SOCIETY
Communication
pubs.acs.org/JACS

Lateral Growth of Composition Graded Atomic Layer $MoS_{2(1-x)}Se_{2x}$ Nanosheets

Honglai Li,[†,§] Qinglin Zhang,[†,§] Xidong Duan,[†] Xueping Wu,[†] Xiaopeng Fan,[†] Xiaoli Zhu,[†] Xiujuan Zhuang,[†] Wei Hu,[†] Hong Zhou,[†] Anlian Pan,*[,†] and Xiangfeng Duan*[,‡]

[†]Key Laboratory for Micro-Nano Physics and Technology of Hunan Province, School of Physics and Electronic Science, and State Key Laboratory of Chemo/Biosensing and Chemometrics, Hunan University, Changsha, Hunan 410082, P. R. China

[‡]Department of Chemistry and Biochemistry, University of California, Los Angeles, California 90095, United States

Supporting Information

ABSTRACT: Band gap engineering of transition-metal dichalcogenides is an important task for their applications in photonics, optoelectronics, and nanoelectronics. We report for the first time the continuous lateral growth of composition graded bilayer $MoS_{2(1-x)}Se_{2x}$ alloys along single triangular nanosheets by an improved chemical vapor deposition approach. From the center to the edge of the nanosheet, the composition can be gradually tuned from $x = 0$ (pure MoS_2) to $x = 0.68$, leading to the corresponding bandgap being continuously modulated from 1.82 eV (680 nm) to 1.64 eV (755 nm). Local photoluminescence scanning from the center to the edge gives single band edge emission peaks, indicating high crystalline quality for the achieved alloy nanosheets, which was further demonstrated by the microstructure characterizations. These novel 2D structures offer an interesting system for probing the physical properties of layered materials and exploring new applications in functional nanoelectronic and optoelectronic devices.

Since the discovery of graphene in 2004, 2D layered materials have attracted considerable attention in the past decade.[1−5] Layered transition-metal dichalcogenides (TMDs), e.g., MoS_2, $MoSe_2$, WS_2, and WSe_2, are burgeoning 2D semiconductor materials for their unique electronic and optical properties.[6−22] Since the application of semiconductor materials is closely related to their bandgaps, a vital task in TMDs research is to realize the growth of new 2D materials with tunable bandgaps for potential applications in functional electronic/optoelectronic devices. Bandgap engineering of TMDs has recently been reported by creating composition mixed alloys between TMDs with different bandgaps.[23−25] Composition tunability within single TMD nanostructures has also been reported recently but is limited in heterostructures[26−28] with only two different compositions/bandgaps. Wider-range bandgap engineering with composition largely modulated within single TMD nanostructures is of great significance in constructing high-performance or multifunctional 2D nanodevices, but it remains a challenge to date.

Atomic layered MoS_2 and $MoSe_2$ have direct bandgaps of 1.837 and 1.557 eV and can emit light at room temperature with the spectral peak positions at ∼675 and ∼795 nm, respectively. Due to the similarity in the atomic structure of MoS_2 and $MoSe_2$, ternary $MoS_{2(1-x)}Se_{2x}$ alloy with composition-dependent (x) band gaps is possible to create.[29] Here, using a simple moving source chemical vapor deposition (CVD) method introduced in ref 30, the synthesis of composition graded $MoS_{2(1-x)}Se_{2x}$ alloy nanosheets was achieved for the first time. From the center to the edge along such a single nanosheet, the composition can be continuously tuned from $x = 0$ (pure MoS_2) to $x = 0.68$, leading to the corresponding bandgap being gradually modulated from 1.82 eV (680 nm) to 1.64 eV (755 nm). These new 2D semiconductor nanostructures may find potential applications in integrated nanoelectronics and nanophotonics.

For the growth of these composition graded 2D nanostructures, an improved CVD approach[30] was used. An alumina boat loaded with MoO_3 powder was placed at the heating center of a quartz tube, and at the upstream of the tube, two other boats loaded with sulfur and selenium powder, respectively, were placed, which can be shifted by two quartz rods driven by step motors through magnetic force during the growth, respectively (Figure S1). On the alumina boat with MoO_3 powder, three pieces of Si wafers (with 300 nm SiO_2) were placed. Before heating, Ar mixed with 5% H_2 gas was first introduced into the system for 10 min and maintained the pressure at 15 Torr. The furnace was then heated at a rate of 30 °C/min from room temperature to 780 °C. After 1 min of growth at this temperature, the selenium powder was then shifted downstream (toward the furnace center) slowly from room temperature area to the region (∼240 °C) for the evaporation of selenium, and the sulfur powder was concomitantly shifted upstream until it could not evaporate any more, with the temperature of the furnace reduced to 720 °C at a rate of 10 °C/min. Continuing the growth for 3 min, the furnace was naturally cooled to room temperature.

With this approach, a lateral composition graded ternary $MoS_{2(1-x)}Se_{2x}$ can in principle be synthesized by an effective control of the vaporization of the source materials through a lateral epitaxial process, as shown schematically in Figure 1a. The resulting lateral composition graded $MoS_{2(1-x)}Se_{2x}$ nanosheets predominantly exhibit a well-faceted regular triangle geometry. Figure 1b shows the optical image of a typical MoS_2 triangular nanosheet (seed) grows for just 1 min at 780 °C.

Received: February 12, 2015
Published: April 14, 2015

DOI: 10.1021/jacs.5b01594
J. Am. Chem. Soc. 2015, 137, 5284−5287

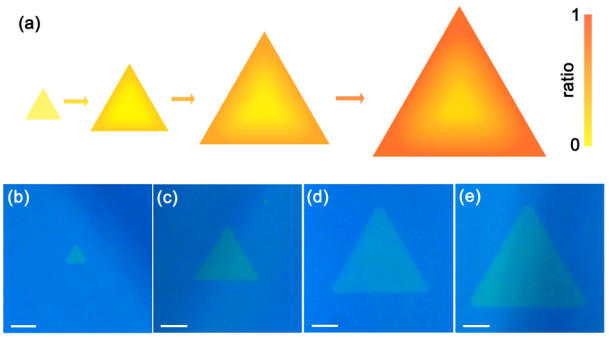

Figure 1. (a) Schematic diagram of the growth process of the lateral composition graded $MoS_{2(1-x)}Se_{2x}$ nanosheets [ratio: Se/(S + Se)]. (b–e) Optical images of representative single $MoS_{2(1-x)}Se_{2x}$ nanosheets at four different growth stages with the growth time of 1, 3, 7, and 10 min, respectively (scale bars, 5 μm).

Due to the existence of dangling bonds, the edge of the preformed MoS_2 nanosheet would act as the growth front, leading to the extension of the seed in the lateral under the followed growth. When the selenium powder started to evaporate, more and more Se atoms (and less and less S atoms) react with MoO_3, resulting in the growth of composition graded $MoS_{2(1-x)}Se_{2x}$ alloy in the lateral direction of the nanosheet, as seen in Figure 1c–e, showing the representative single nanosheets with the growth times of 3, 7, and 10 min, respectively. The results indicate that the nanosheets grow larger and larger in the lateral direction with increasing reaction time.

Figure 2a shows a typical transmission electron microscopy (TEM) image of a representative nanosheet with a uniform thickness of 1.65 nm, indicating bilayer character of the sheet (see Figure S2 in the Supporting Information). Figure 2b plots

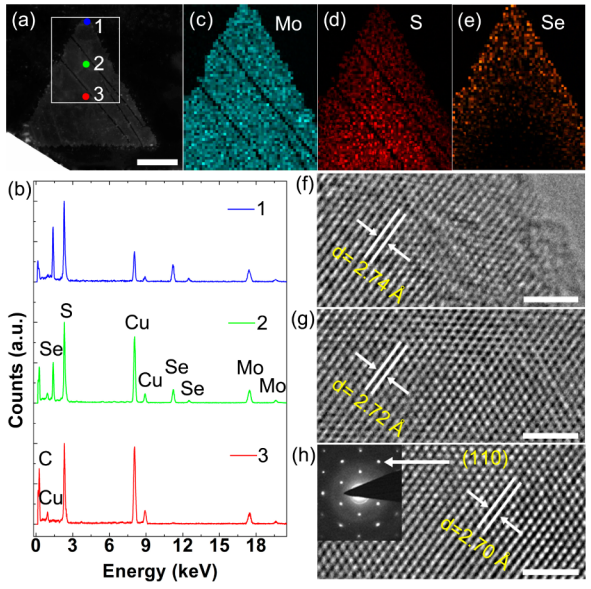

Figure 2. (a) Typical TEM image of the obtained ternary $MoS_{2(1-x)}Se_{2x}$ nanosheets (scale bar, 3 μm) and (b) the corresponding TEM-EDX profiles recorded at three different positions (1–3) in the sheet. (c–e) 2D elemental mapping for the three detected elements: Mo, S, and Se, respectively. (f–h) The HRTEM images taken from the three positions (scale bars, 2 nm). Inset of (h): the SAED pattern of the nanosheet.

the energy dispersive X-ray (EDX) spectroscopy spectra collected from three positions (dots 1–3 in Figure 2a), indicating that the nanosheet consists of elements S, Se, and Mo and the ratio of Se/S increases gradually from positions 3 to 1, demonstrating the existence of graded composition within the as-grown nanosheets. Figure 2c–e further shows the two-dimensional (2D) elemental mapping for the detected elements of Mo, S, and Se, respectively, in a selected region of this sheet (marked with a white rectangle in Figure 2a). It is evident that Mo is uniformly distributed across the whole region, while S is located more at the center with reducing signal toward the edge region of the sheet, and Se shows the opposite trend with essentially zero signal at the center and increasing signal toward the edge region. The elemental analyses further demonstrate that these nanosheets are laterally graded in composition.

Figure 2f–h shows the high-resolution TEM (HRTEM) images taken from the three different positions along the nanosheet, corresponding to the positions for the EDX analysis (see Figure 2a,b), which shows that all the examined positions are highly crystallized, with the measured lattice plane spacings of 2.74, 2.72, and 2.70 Å, respectively, in agreement with the (100) plane spacing of the composition tunable atomic layered $MoS_{2(1-x)}Se_{2x}$ alloys.[31] The inset of Figure 2h is the selected area electron diffraction (SAED) pattern of the sheet, which shows a clearly defined single set of diffraction spots, further demonstrating the single-crystalline nature of the achieved 2D structures without significant defects.

Figure 3a shows the position-dependent photoluminescence (PL) spectra of a single composition graded $MoS_{2(1-x)}Se_{2x}$

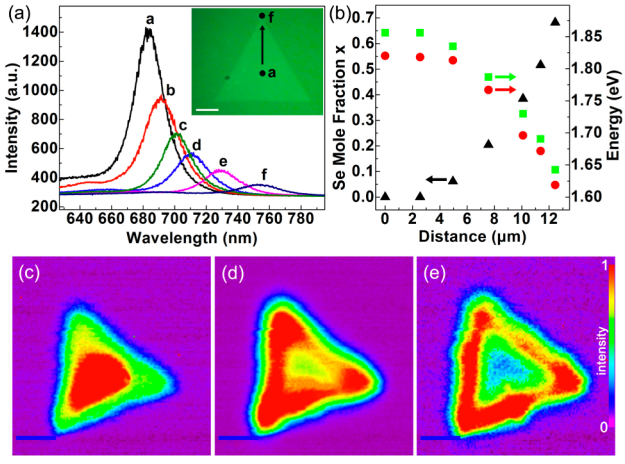

Figure 3. (a) Position-dependent PL spectrum of a lateral composition graded $MoS_{2(1-x)}Se_{2x}$ nanosheet and optical image (inset: scale bar, 5 μm). (b) Position-dependent compositions and bandgap values of the sheet. (c–e) Wavelength-dependent PL mapping of a single composition graded nanosheet in the spectral regions of 680–690, 710–720, 750–760 nm, respectively (scale bars, 5 μm).

nanosheet excited by a 488 nm Ar^+ laser. The spectra (a to f) were collected locally from several representative positions along the indicated arrow from the center to the edge of the nanosheet, as seen from the inset of the figure. All the spectra reveal single emission bands, with the peak wavelength gradually red-shifted when the detecting spot is moved from the center (a) to the edge (f). The position-dependent spectral feature and evolution of these $MoS_{2(1-x)}Se_{2x}$ nanosheets is well consistent with the composition-dependent band edge emission of $MoS_{2(1-x)}Se_{2x}$ atomic layered thin films.[31] The correspond-

DOI: 10.1021/jacs.5b01594
J. Am. Chem. Soc. 2015, 137, 5284–5287

ing position-dependent compositions and bandgap values are given in Figure 3b. The Se mole fraction [x, Se/(S + Se)] values (black triangles) are obtained from the EDS examinations. It is found that the bandgap values converted from the PL spectra (red circles) are in good consistency with those (green rectangles) obtained from the calculation according the bandgap relation:

$$E_g(x) = xE_g(MoSe_2) + (1 - x)E_g(MoS_2) - bx(1 - x) \quad (1)$$

This indicates that all the observed PL are from the band-edge emission, which is modulated with the continuous variation of the composition from the center to the edge of the nanosheets. The observation of single band-edge emission, with few defects or structural disorder-related low-energy emission detected, further indicates that all the area within the nanosheets are highly crystallized, which is consistent with the HRTEM observations. PL mapping measurement was used to further investigate the spatial composition or bandgap distribution in the $MoS_{2(1-x)}Se_{2x}$ nanosheets. Figure 3c–e gives the wavelength-selected PL emission mapping of the examined nanosheet in the spectral regions of 680–690, 710–720, 750–760 nm, respectively. Obviously, the short wavelength region (680–690 nm) is mainly located at the center of the nanosheet, while the long wavelength region (750–760 nm) is mostly located around the edge of sheet. This observation is consistent with the above composition and bandgap investigations and further demonstrates the $MoS_{2(1-x)}Se_{2x}$ atomic layers are composition graded along the whole plane of the sheet from the center to the edge.

The formation of composition graded single $MoS_{2(1-x)}Se_{2x}$ nanosheets can further be confirmed by the composition-dependent vibration modes observed from the micro-Raman measurements. Figure 4a plots the normalized position-dependent Raman spectra, scanning from the center (curves a) to the edge (curves f) of the nanosheet shown in the inset of Figure 3a. The results show that the modes related to Se–Mo [$A_{1g(Se-Mo)}$, $E_{2g(Se-Mo)}$] are absent at the center, which will come out and with their intensities gradually turning stronger when the detection spot scanned from the center to the edge. However, the modes related to S–Mo [$E_{2g(S-Mo)}$, $A_{1g(S-Mo)}$] are very strong at the central region, with the intensity gradually decreasing from the center toward the edge, contrary to those of the Se–Mo related modes. This transition of molecular vibration modes shows good agreement with the continuously increased (decreased) of the Se (S) contents from the center to the edge in these lateral composition graded $MoS_{2(1-x)}Se_{2x}$ alloys. In the meantime, it is found that from positions a to f, all the vibration modes shift to low frequency (Figure 4b). As the frequencies of vibration modes related to Se–Mo locate lower than that of S–Mo (shown in Figure 4a), when the Se (S) contents are gradually increased (decreased), the modes related to S–Mo would be softened by the interactions between Se and S atoms, and modes related to Se–Mo would be reinforced on the contrary, eventually leading to the low shift in their frequencies.[23]

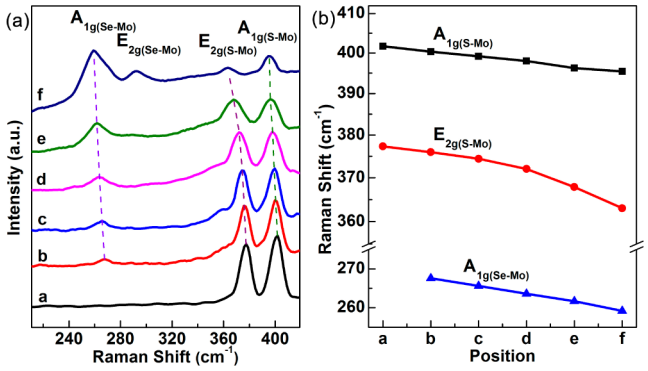

Figure 4. (a) Position-dependent micro-Raman spectra of the lateral composition graded nanosheet shown in the inset of Figure 3a. (b) The Raman modes shift with the positions along the nanosheet.

In summary, lateral composition graded atomic layered 2D $MoS_{2(1-x)}Se_{2x}$ nanosheets have been successfully synthesized using a simple moving source thermal evaporation method by an improved CVD route. Both microstructure and spectral characterizations demonstrate that the achieved nanosheets are highly crystallized, with the composition being continuously tuned from the pure MoS_2 at the center ($x = 0$) to a highly Se-doped ternary alloy at the edge ($x = 0.68$). These alloy nanosheets can give position-related PL emission, with the peak position broadly tunable from 680 nm at the center to 755 nm at the edge. These bandgap modulated 2D alloy nanostructures could find significant applications in fundamental physical research and the construction of functional electronic and photoelectric devices.

■ ASSOCIATED CONTENT

Supporting Information

Experimental details and characterization data. This material is available free of charge via the Internet at http://pubs.acs.org.

■ AUTHOR INFORMATION

Corresponding Authors

*anlian.pan@hnu.edu.cn
*xduan@chem.ucla.edu

Author Contributions

§These authors contributed equally.

Notes

The authors declare no competing financial interest.

■ ACKNOWLEDGMENTS

The authors are grateful to the NSF of China (nos.11374092, 11204073, 61474040 and 51302077), the National Basic Research Program of China (no. 2012CB932703), the Hunan province science and technology plan (nos. 2014FJ2001, 2014GK3015 and 2014TT1004), and the Hunan Provincial Natural Science Foundation of China (no.2015JJ3049).

■ REFERENCES

(1) Zhang, L.; Yu, J.; Yang, M.; Xie, Q.; Peng, H.; Liu, Z. *Nat. Commun.* **2013**, *4*, 1443.
(2) Freitag, M.; Low, T.; Zhu, W.; Yan, H.; Xia, F.; Avouris, P. *Nat.Commun.* **2013**, *4*, 1951.
(3) Weiss, N. O.; Zhou, H.; Liao, L.; Liu, Y.; Jiang, S.; Huang, Y.; Duan, X. *Adv. Mater.* **2012**, *24*, 5782.
(4) Yan, K.; Wu, D.; Peng, H.; Jin, L.; Fu, Q.; Bao, X.; Liu, Z. *Nat. Commun.* **2012**, *3*, 1280.
(5) Yan, H.; Li, X.; Chandra, B.; Tulevski, G.; Wu, Y.; Freitag, M.; Zhu, W.; Avouris, P.; Xia, F. *Nat. Nanotechnol.* **2012**, *7*, 330.
(6) Halim, U.; Zheng, C. R.; Chen, Y.; Lin, Z.; Jiang, S.; Cheng, R.; Huang, Y.; Duan, X. *Nat. Commun.* **2013**, *4*, 2213.

DOI: 10.1021/jacs.5b01594
J. Am. Chem. Soc. 2015, 137, 5284–5287

(7) Yu, Z.; Pan, Y.; Shen, Y.; Wang, Z.; Ong, Z.; Xu, T.; Xin, R.; Pan, L.; Wang, B.; Sun, L.; Wang, J.; Zhang, G.; Zhang, Y. W.; Shi, Y.; Wang, X. *Nat. Commun.* **2014**, *5*, 5290.
(8) Zhou, H.; Yu, F.; Liu, Y.; Zou, X.; Cong, C.; Qiu, C.; Yu, T.; Yan, Z.; Shen, X.; Sun, L.; Boris, I. Y.; James, M. T. *Nano Res.* **2013**, *6*, 703.
(9) Yin, Z. Y.; Chen, B.; Bosman, M.; Cao, X. H.; Chen, J. Z.; Zheng, B.; Zhang, H. *Small* **2014**, *10*, 3537.
(10) Xu, X.; Yao, W.; Xiao, D.; Heinz, T. F. *Nat. Phys.* **2014**, *10*, 343.
(11) Shaw, J. C.; Zhou, H.; Chen, Y.; Weiss, N. O.; Liu, Y.; Huang, Y.; Duan, X. *Nano Res.* **2014**, *7*, 511.
(12) Yu, W. J.; Li, Z.; Zhou, H.; Chen, Y.; Wang, Y.; Huang, Y.; Duan, X. *Nat. Mater.* **2013**, *12*, 246.
(13) Qiu, H.; Xu, T.; Wang, Z.; Ren, W.; Nan, H.; Ni, Z.; Chen, Q.; Yuan, S.; Miao, F.; Song, F.; Long, G.; Shi, Y.; Sun, L.; Wang, J.; Wang, X. *Nat. Commun.* **2013**, *4*, 2642.
(14) Yang, D.; Lu, Z. Y.; Rui, X. H.; Huang, X.; Li, H.; Zhu, J. X.; Zhang, W. Y.; Lam, Y. M.; Hng, H. H.; Zhang, H.; Yan, Q. Y. *Angew. Chem., Int. Ed.* **2014**, *53*, 9352.
(15) Nie, Z. G.; Long, R.; Sun, L. F.; Huang, C. C.; Zhang, J.; Xiong, Q. H.; Hewak, D. W.; Shen, Z. X.; Prezhdo, O. V.; Loh, Z. H. *ACS Nano* **2014**, *8*, 10931.
(16) Jones, A. M.; Yu, H.; Ross, J. S.; Klement, P.; Ghimire, N. J.; Yan, J.; Mandrus, D. G.; Yao, W.; Xu, X. *Nat. Phys.* **2014**, *10*, 130.
(17) Yang, Y.; Fei, H.; Ruan, G.; Xiang, C.; James, M. T. *Adv. Mater.* **2014**, *26*, 8163.
(18) Gong, C.; Huang, C.; Miller, J.; Cheng, L.; Hao, Y.; Cobden, D.; Kim, J.; Ruoff, R. S.; Wallace, R.; Cho, K.; Xu, X.; Chabal, Y. *ACS Nano* **2013**, *7*, 11350.
(19) Utama, M. I. B.; Lu, X.; Yuan, Y. W.; Xiong, Q. H. *Appl. Phys. Lett.* **2014**, *105*, 253102.
(20) Ross, J. S.; Klement, P.; Jones, A. M.; Ghimire, N. J.; Yan, J.; Mandrus, D. G.; Taniguchi, T.; Watanabe, K.; Kitamura, K.; Yao, W.; Cobden, D. H.; Xu, X. *Nat. Nanotechnol.* **2014**, *9*, 268.
(21) Li, H.; Wu, J.; Yin, Z.; Zhang, H. *Acc. Chem. Res.* **2014**, *47*, 1067.
(22) Huang, X.; Tan, C.; Yin, Z.; Zhang, H. *Adv. Mater.* **2014**, *26*, 2185.
(23) Li, H.; Duan, X.; Wu, X.; Zhuang, X.; Zhou, H.; Zhang, Q.; Zhu, X.; Hu, W.; Fan, X.; Wang, X.; Xu, J.; Pan, A.; Duan, X. *J. Am. Chem. Soc.* **2014**, *136*, 3756.
(24) Dumcenco, D. O.; Kobayashi, H.; Liu, Z.; Huang, Y. S.; Suenaga, K. *Nat. Commun.* **2013**, *4*, 1351.
(25) Tongay, S.; Narang, D. S.; Kang, J.; Fan, W.; Ko, C. H.; Luce, A. V.; Wang, K. X.; Suh, J.; Patel, K. D.; Pathak, V. M.; Li, J. B.; Wu, J. Q. *Appl. Phys. Lett.* **2014**, *104*, 012101.
(26) Duan, X.; Wang, C.; Shaw, J. C.; Cheng, R.; Chen, Y.; Li, H.; Wu, X.; Tang, Y.; Zhang, Q.; Pan, A.; Jiang, J.; Yu, R.; Huang, Y.; Duan, X. *Nat. Nanotechnol.* **2014**, *9*, 1024.
(27) Cheng, R.; Li, D.; Zhou, H.; Wang, C.; Yin, A.; Jiang, S.; Liu, Y.; Chen, Y.; Huang, Y.; Duan, X. *Nano Lett.* **2014**, *14*, 5590.
(28) Yu, W. J.; Li, Z.; Zhou, H.; Chen, Y.; Wang, Y.; Huang, Y.; Duan, X. *Nat. Mater.* **2013**, *12*, 246.
(29) Komsa, H.-P.; Krasheninnikov, A. V. *J. Phys. Chem. Lett.* **2012**, *3*, 3652.
(30) Gu, F.; Yang, Z.; Yu, H.; Xu, J.; Wang, P.; Tong, L.; Pan, A. *J. Am. Chem. Soc.* **2011**, *133*, 2037.
(31) Kang, J.; Tongay, S.; Li, J.; Wu, J. *J. Appl. Phys.* **2013**, *113*, 143703.

DOI: 10.1021/jacs.5b01594
J. Am. Chem. Soc. 2015, 137, 5284−5287